Chemical Science

ROYAL SOCIETY OF CHEMISTRY

EDGE ARTICLE

View Article Online
View Journal

Cite this: DOI: 10.1039/d5sc09281g

All publication charges for this article have been paid for by the Royal Society of Chemistry

Regulating red-shifted phosphorescence of carbon dots *via* introducing magnesium chloride

Yibin Long,[a] Haoda Zhang,[a] Yongjin Chen *[b] and Xiaoming Yang *[a]

Received 27th November 2025
Accepted 13th February 2026

DOI: 10.1039/d5sc09281g

rsc.li/chemical-science

Achieving the multicolor phosphorescence of carbon dots (CDs), particularly with controllable wavelengths, remains a challenging yet desirable goal. Herein, we designed and prepared phosphorescent CDs (CDs@Al_2O_3 and CDs@$MgAl_2O_4$) using an *in situ* synthesis strategy. The oxygen vacancies in CDs stabilized the triplet excitons, thus enabling the long-lived and strong phosphorescence of these CDs. Importantly, CDs@$MgAl_2O_4$ exhibited obviously red-shifted phosphorescence (552 nm) compared to CDs@Al_2O_3 (525 nm) owing to increased conjugation and a narrowed bandgap, with the narrowed gap derived from coordination between magnesium and C=O. These CDs showed excitation-dependent phosphorescence, which was tunable from cyan to red by varying excitation wavelengths. Additionally, we synthesized a series of phosphorescent CDs by employing different carbon sources, among which the magnesium-doped CDs consistently displayed red-shifted phosphorescence, thus proving the universality of this strategy and providing an innovative approach for regulating the phosphorescence of CDs.

1. Introduction

Room-temperature phosphorescence (RTP) materials have garnered significant research interest due to their distinctive optical characteristics, such as a large Stokes shift, high signal-to-noise ratios and persistent luminescence after excitation cessation.[1–3] These properties have enabled their extensive utilization across diverse fields including optoelectronic devices, advanced anti-counterfeiting, high-resolution bioimaging, multifunctional sensing platforms and beyond.[4–7] Nevertheless, conventional RTP materials, encompassing pure organic compounds, metal–organic complexes and rare-earth-doped phosphors, are plagued by multiple disadvantages such as inherent cytotoxicity restricting biomedical applications,[1,8] complex preparation process,[9] and vulnerability of triplet excitons to oxygen-induced quenching or thermal deactivation mechanisms,[10] all of which undoubtedly hinder their practical applications. Consequently, acquiring RTP materials with cost-effectiveness, simple preparation procedures and high environmental tolerance remains challenging, and thus the precise regulation of the phosphorescent emissions of RTP materials is highly valuable.

Carbon dots (CDs), as a class of zero-dimensional carbon-based luminescent nanomaterials, have attracted much attention due to their diverse optical characteristics, such as fluorescence,[11] phosphorescence[12] and thermally activated delayed fluorescence.[13] These properties originate from their unique electronic and surface structures. Compared with traditional room-temperature phosphorescent materials, CDs offer distinct advantages including easy preparation,[14] economic viability,[15] low biological toxicity[16] and no reliance on rare-earth elements, which not only enhance the practicality of CD-based RTP materials but also highlight their potential to serve as promising phosphorescent alternatives.

Currently, there are two major strategies to realize RTP emission in CD-based materials. The first strategy is rigid matrix engineering, such as polymer chain entanglement[17] and introduction of matrices (SiO_2,[18] B_2O_3,[19,20] urea[21] or PVA[13]), which suppress the rotation and vibration of CDs or non-radiative transitions, thus enabling RTP emission.[22] The second strategy involves doping heteroatoms such as B, N, P or S to regulate the electronic cloud.[23,24] These dopants could enhance spin–orbit coupling (SOC) through heavy-atom effects, which also facilitates efficient intersystem crossing (ISC) by breaking spin-forbidden and increasing the overlap between singlet and triplet energy levels.[25] Nitrogen doping, for instance, could suppress the spin-forbidden transition and promote the effective filling of triplet excitons, thereby enhancing the long-lived RTP of CDs.[26] Although numerous methods have been developed to achieve RTP in CD-based materials, their RTP is mainly concentrated in the short-wavelength range from blue to green.[27] It is still a challenge to obtain CD-based RTP materials with controllable emissions.

In this work, we successfully developed an in situ strategy to prepare multicolor RTP CDs by introducing $AlCl_3$ and $MgCl_2$,

[a]College of Pharmaceutical Sciences, Southwest University, Chongqing 400715, P. R. China. E-mail: ming4444@swu.edu.cn

[b]Center for High Pressure Science and Technology Advanced Research (HPSTAR), Beijing 100193, P. R. China. E-mail: yongjin.chen@hpstar.ac.cn

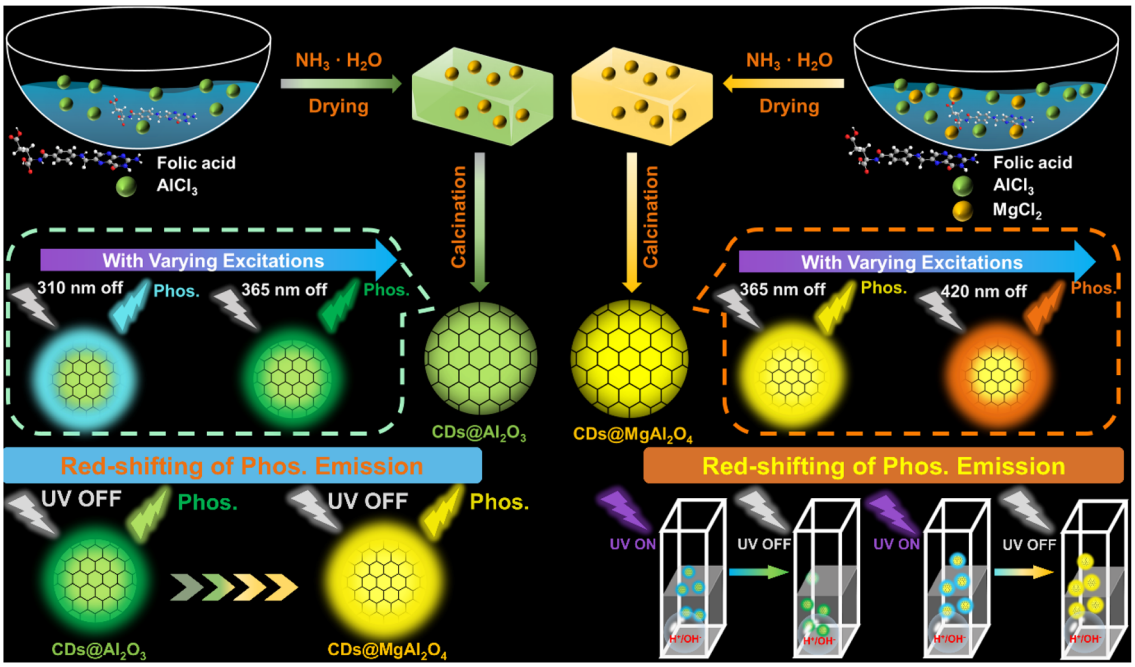

Scheme 1 Illustration of the synthesis and phosphorescence properties of CDs@Al_2O_3 and CDs@$MgAl_2O_4$.

denoted as CDs@Al_2O_3 and CDs@$MgAl_2O_4$. The rigid framework and abundant oxygen vacancies effectively stabilized the triplet states of CDs, thus resulting in persistent phosphorescence even under extremely acidic or basic conditions. To be specific, magnesium incorporation in CDs@$MgAl_2O_4$ leads to narrowing of the optical band gap, further resulting in red-shifted phosphorescence compared to CDs@Al_2O_3, which lacks magnesium. Ultimately, a series of CDs with multicolor RTP were synthesized by varying the carbon source, thus proving the universality of this proposed approach (Scheme 1).

2. Results and discussion

2.1. Preparation and optical properties of CDs@Al_2O_3 and CDs@$MgAl_2O_4$

Boric acid has been employed to prepare room-temperature phosphorescent CDs due to its unique electronic properties. Nevertheless, its structural instability with fluctuated humidity and temperature presents obvious limitations. In contrast, aluminum has a similar electronic structure to boron, and its structure is more stable and exhibits a higher environmental tolerance than boron. Therefore, we here selected folic acid and aluminum chloride as the raw materials to prepare CDs@Al_2O_3. Subsequently, to optimize the performance of CDs@Al_2O_3, we systematically investigated the potential effects of raw material ratios, calcination temperature, and calcination time on its phosphorescence properties. The experimental results indicated that these factors obviously affected the phosphorescence intensity of CDs@Al_2O_3 (Fig. S1), while scarcely affecting the wavelength (Fig. S2). In order to regulate the RTP emission wavelength of CDs, we attempted to change the elemental composition and the electronic cloud density of CDs by introducing magnesium, an alkaline-earth metal element with high charge density, and further synthesized CDs@$MgAl_2O_4$ using the same way as preparing CDs@Al_2O_3.

The fluorescence and phosphorescence spectra of CDs@Al_2O_3 and CDs@$MgAl_2O_4$ were initially recorded, and both the corresponding powders exhibited strong fluorescence and RTP. The maximal fluorescence emissions of CDs@Al_2O_3 and CDs@$MgAl_2O_4$ were separately measured at 415 nm and 427 nm (Fig. 1a and b) as well as their CIE coordinates shown in Fig. 1c. Subsequently, we recorded the phosphorescence spectra of CDs@Al_2O_3 and CDs@$MgAl_2O_4$ excited with light of 365 nm and 420 nm (Fig. 1d and e), respectively. Particularly, CDs@Al_2O_3 exhibited green phosphorescence at 525 nm under 365 nm excitation and was visible to the naked eye for approximately 10 s, while CDs@$MgAl_2O_4$ emitted yellow phosphorescence at 552 nm, persisting for around 8 s (Fig. 1h). Under 420 nm excitation, CDs@Al_2O_3 showed visible yellow phosphorescence at 565 nm lasting for 5 s, while CDs@$MgAl_2O_4$ emitted orange phosphorescence at 583 nm that was visible for around 6 s under the same excitation (Fig. 1i). Fig. 1f shows the CIE coordinates of the phosphorescence emission of CDs@Al_2O_3 and CDs@$MgAl_2O_4$ as the excitation wavelengths were 365 nm and 420 nm, indicating that the phosphorescent emission wavelengths of these two CDs were obviously affected by the excitation wavelengths. Notably, both CDs@Al_2O_3 and CDs@$MgAl_2O_4$ exhibited phosphorescence emissions under visible light excitation.

The previous phenomena indicated that the phosphorescence emission wavelengths of CDs@Al_2O_3 and CDs@$MgAl_2O_4$ were strongly excitation-dependent. To systematically explore this excitation dependency, we further recorded the phosphorescence spectra of CDs@Al_2O_3 and CDs@$MgAl_2O_4$ under

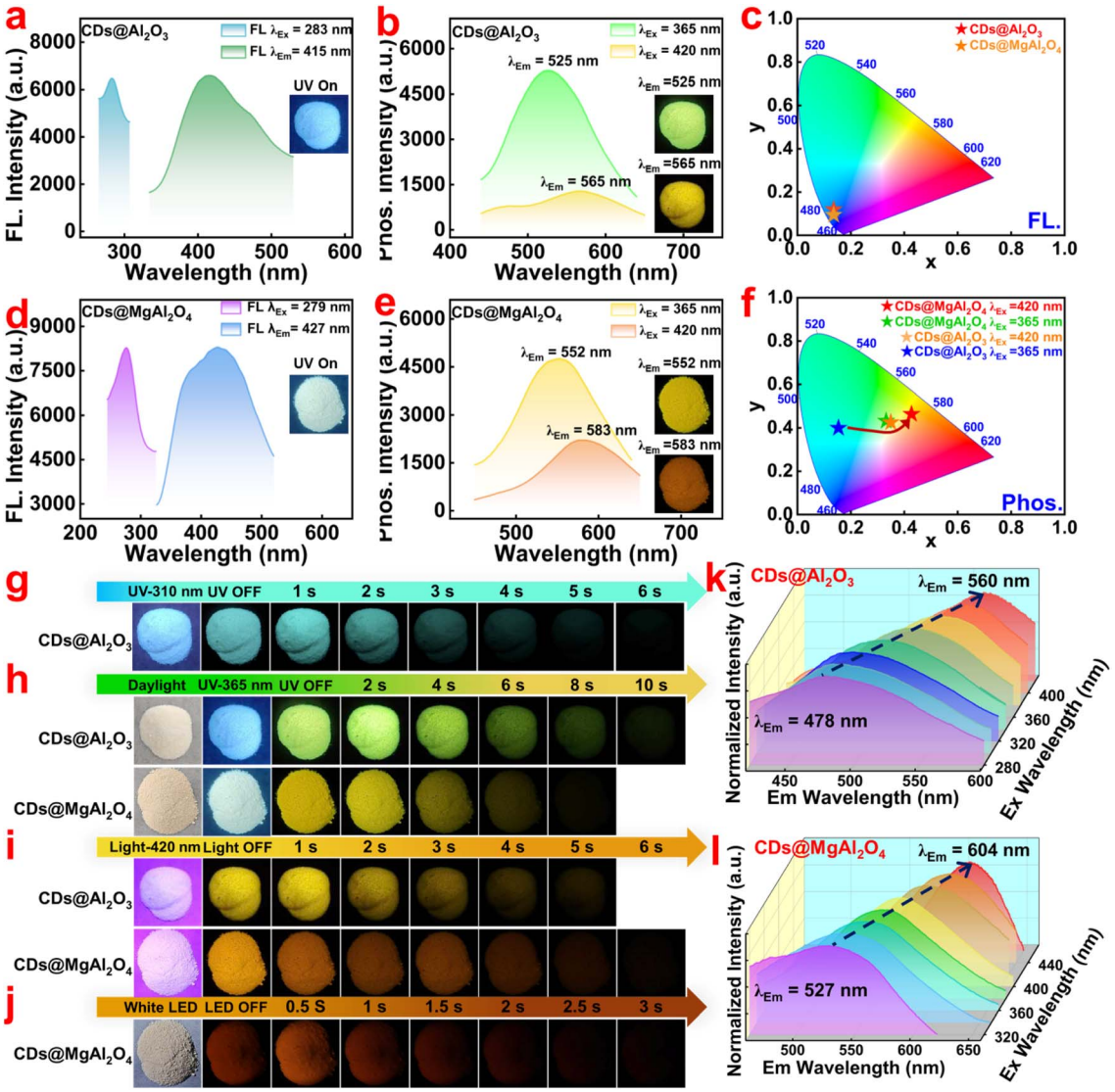

Fig. 1 Fluorescence excitation and emission spectra of CDs@Al_2O_3 (a) and CDs@$MgAl_2O_4$ (d). (c) Fluorescent CIE coordinates of CDs@Al_2O_3 and CDs@$MgAl_2O_4$. Phosphorescence emission spectra of CDs@Al_2O_3 (b) and CDs@$MgAl_2O_4$ (e) under excitation at 365 nm and 420 nm. (f) Phosphorescent CIE coordinates of CDs@Al_2O_3 and CDs@$MgAl_2O_4$. (g) Images of CDs@Al_2O_3 under 310 nm UV irradiation and after the UV light was turned off. (h) Images of CDs@Al_2O_3 and CDs@$MgAl_2O_4$ under daylight, 365 nm UV irradiation and after the UV light was turned off. (i) Images of CDs@Al_2O_3 and CDs@$MgAl_2O_4$ under 420 nm excitation and after the light was turned off. (j) Images of CDs@$MgAl_2O_4$ under WLED irradiation and after the WLED was turned off. Phosphorescence spectra of CDs@Al_2O_3 (k) and CDs@$MgAl_2O_4$ (l) under excitation at various wavelengths.

excitation at varied wavelengths (Fig. 1k and l). The results showed that the phosphorescence emission wavelength of CDs@Al_2O_3 showed a red-shift as the excitation wavelength increased from 280 nm to 420 nm. We selected 310 nm as the representative excitation wavelength, under which CDs@Al_2O_3 exhibited obvious cyan phosphorescence at 480 nm (Fig. 1g and S3). Similarly, the phosphorescence emission of CDs@$MgAl_2O_4$ exhibited a red-shift when the excitation wavelength increased from 320 nm to 460 nm (Fig. 1l). Importantly, the phosphorescence of CDs@$MgAl_2O_4$ exhibited a distinct red shift compared to that of CDs@Al_2O_3 under the same excitation, and both of them could emit phosphorescence under visible light excitation. Furthermore, CDs@$MgAl_2O_4$ uniquely exhibited red phosphorescence under white light-emitting diode (WLED) excitation without requiring ultraviolet light, thus highlighting its great potential for visible light activated phosphorescence (Fig. 1j). Therefore, CDs@Al_2O_3 and CDs@$MgAl_2O_4$ with successive and tunable room-temperature phosphorescence (RTP) were successfully achieved *via* modulating the excitation wavelengths.

2.2. Structural characterization

To elucidate the luminescence mechanism of CDs@Al_2O_3 and CDs@$MgAl_2O_4$, their systematic structural characterization was conducted through multiple analytical techniques. The morphologies of the two CDs were initially observed using HR-

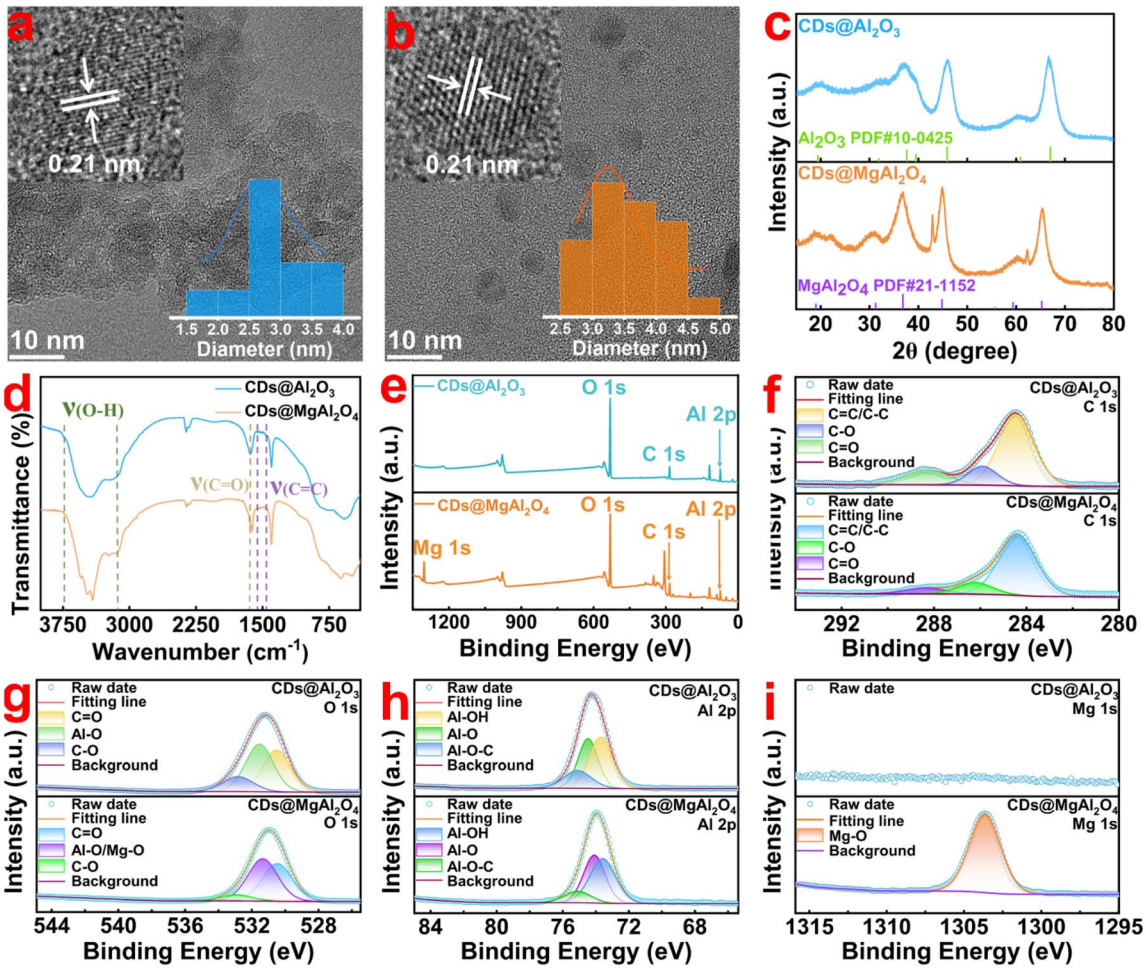

Fig. 2 TEM images of $CDs@Al_2O_3$ (a) and $CDs@MgAl_2O_4$ (b). Inset: HR-TEM images and particle size distributions. (c) XRD patterns of $CDs@Al_2O_3$ and $CDs@MgAl_2O_4$. (d) FTIR spectra of $CDs@Al_2O_3$ and $CDs@MgAl_2O_4$. (e) XPS surveys of $CDs@Al_2O_3$ and $CDs@MgAl_2O_4$. High-resolution XPS spectra of (f) C 1s, (g) O 1s, (h) Al 2p and (i) Mg 1s.

TEM, followed by obtaining their size distributions. The TEM images revealed that the formation of CDs and the average particle sizes of $CDs@Al_2O_3$ and $CDs@MgAl_2O_4$ were determined to be 2.83 nm and 3.50 nm, respectively (Fig. 2a and b). Meanwhile, the HR-TEM images showed distinct lattice fringes in both CDs with the same lattice spacing of 0.21 nm (Fig. 2a and b), and this spacing aligned with the (100) crystal plane of graphite,[28] indicating that these CDs retained graphitic-like sp^2 carbon cores. The increased size of $CDs@MgAl_2O_4$ corresponded to the extended sp^2 carbon core, which enhanced the conjugation effects, thus leading to a red shift of the phosphorescence emission. The X-ray diffraction (XRD) patterns of $CDs@Al_2O_3$ exhibited obvious peaks at 46° and 67°, which were consistent with the characteristic peaks of Al_2O_3 (JCPDS No. 10-0425),[29] while the peaks of $CDs@MgAl_2O_4$ corresponded to the characteristic peaks of $MgAl_2O_4$ (JCPDS No. 21-1152) (Fig. 2c).[30] These findings demonstrated the formation of Al_2O_3 for $CDs@Al_2O_3$ as well as $MgAl_2O_4$ for $CDs@MgAl_2O_4$, whose intrinsic crystalline frameworks were possibly responsible for their phosphorescence properties.

Subsequently, FTIR was employed to explore the surface functional groups of $CDs@Al_2O_3$ and $CDs@MgAl_2O_4$ (Fig. 2d). The FTIR spectra of both CDs exhibited a broad and intense stretching vibration band of O–H spanning 3750 cm^{-1} to 3100 cm^{-1}, indicating the presence of hydroxyls originating from surface functionalization or absorbed water.[31] The peaks at 1637 cm^{-1} and 1579–1450 cm^{-1} corresponded to the stretching vibrations of C=O and C=C in the aromatic ring of $CDs@Al_2O_3$, while the stretching vibrations of C=O and C=C in the aromatic ring for $CDs@MgAl_2O_4$ are located at 1618 cm^{-1} and 1550 cm^{-1}–1435 cm^{-1}, respectively. This red-shift suggested the interaction between magnesium ions and C=O of the aromatic skeleton, thus altering their local electronic cloud.[32] The broad bands centered at 840 cm^{-1} and 576 cm^{-1} were associated with the Al–O vibrations of $CDs@Al_2O_3$.[26] In the FTIR spectrum of $CDs@MgAl_2O_4$, the broad peak at 820 cm^{-1} and the sharp peak at 625 cm^{-1} corresponded to the vibration of Al–O, while the peak at 487 cm^{-1} was attributed to the vibration of Mg–O. These findings collectively demonstrated that introducing magnesium affected their structures and magnesium

played a critical role in regulating the phosphorescence of CDs@$MgAl_2O_4$.

XPS was further employed to determine the elemental composition of CDs@Al_2O_3 and CDs@$MgAl_2O_4$. The XPS survey revealed that CDs@Al_2O_3 was mainly composed of C (21.18%), O (51.36%) and Al (27.46%) elements (Fig. 2e), and the peaks at 531.3 eV, 284.9 eV and 74.2 eV referred to the characteristic peaks of O 1s, C 1s and Al 2p, respectively. In contrast, CDs@$MgAl_2O_4$ exhibited characteristic peaks at 74.0 eV (Al 2p), 284.6 eV (C 1s), 531.1 eV (O 1s) and 1303.8 eV (Mg 1s), indicating that it was mainly composed of C (22.66%), O (47.73%), Mg (7.73%), Al (21.37%).[26,33] As for the high-resolution C 1s spectrum of CDs@Al_2O_3, the characteristic peaks at 288.3 eV, 286.0 eV and 284.4 eV corresponded to C=O, C–O and C–C/C=C, respectively (Fig. 2f). Similarly, CDs@$MgAl_2O_4$ showed the same groups of C=O (288.4 eV), C–O (286.2 eV) and C–C/C=C (284.4 eV) (Fig. 2f). Notably, the content of C–C/C=C for CDs@$MgAl_2O_4$ (78.12%) was higher than that for CDs@Al_2O_3 (67.11%), further indicating that CDs@$MgAl_2O_4$ showed a larger sp^2 carbon core. This structural feature resulted in an extended conjugation, thus producing red-shifted phosphorescence. The high-resolution O 1s spectrum of CDs@Al_2O_3 was deconvoluted into three peaks related to C–O (532.8 eV), Al–O (531.5 eV), and C=O (530.5 eV), while the characteristic peaks at 532.8 eV, 531.2 eV and 530.7 eV of CDs@$MgAl_2O_4$ corresponded to C–O, Al–O/Mg–O and C=O, respectively (Fig. 2g). The Al 2p spectrum of CDs@Al_2O_3 was deconvoluted into three peaks of Al–O–C (75.1 eV), Al–O (74.6 eV) and Al–OH (73.8 eV), and CDs@$MgAl_2O_4$ also exhibited three similar peaks of Al–O–C (75.1 eV), Al–O (74.1 eV), and Al–OH (73.6 eV) (Fig. 2h). Differently, the Mg 1s spectrum (Fig. 2i) of CDs@$MgAl_2O_4$ displayed a distinct peak at 1303.6 eV (Mg–O),[34] whereas there was no peak in this range for CDs@Al_2O_3.[33] Taken together, these findings suggested the formation of abundant covalent bonds for the two CDs, which effectively inhibited the non-radiative transitions of excitons, thus promoting the emergence of phosphorescence.

2.3. Generation and regulation of phosphorescence

Remarkably, the phosphorescence emissions of CDs@Al_2O_3 and CDs@$MgAl_2O_4$ were still clearly observed when they were exposed to strong acid (1 M of H_2SO_4) and alkaline (1 M of NaOH) conditions (Fig. 3a and b). The highly tolerant phosphorescence of two CDs was attributed to the rigid bonds of Al–O–C, which not only effectively enhanced ISC efficiency between the singlet and triplet states, but also stabilized the triplet state of CDs.

To further validate the role of folic acid in generating phosphorescence, we performed the same experiments by using $AlCl_3$ or $AlCl_3$–$MgCl_2$ without folic acid. At identical excitation

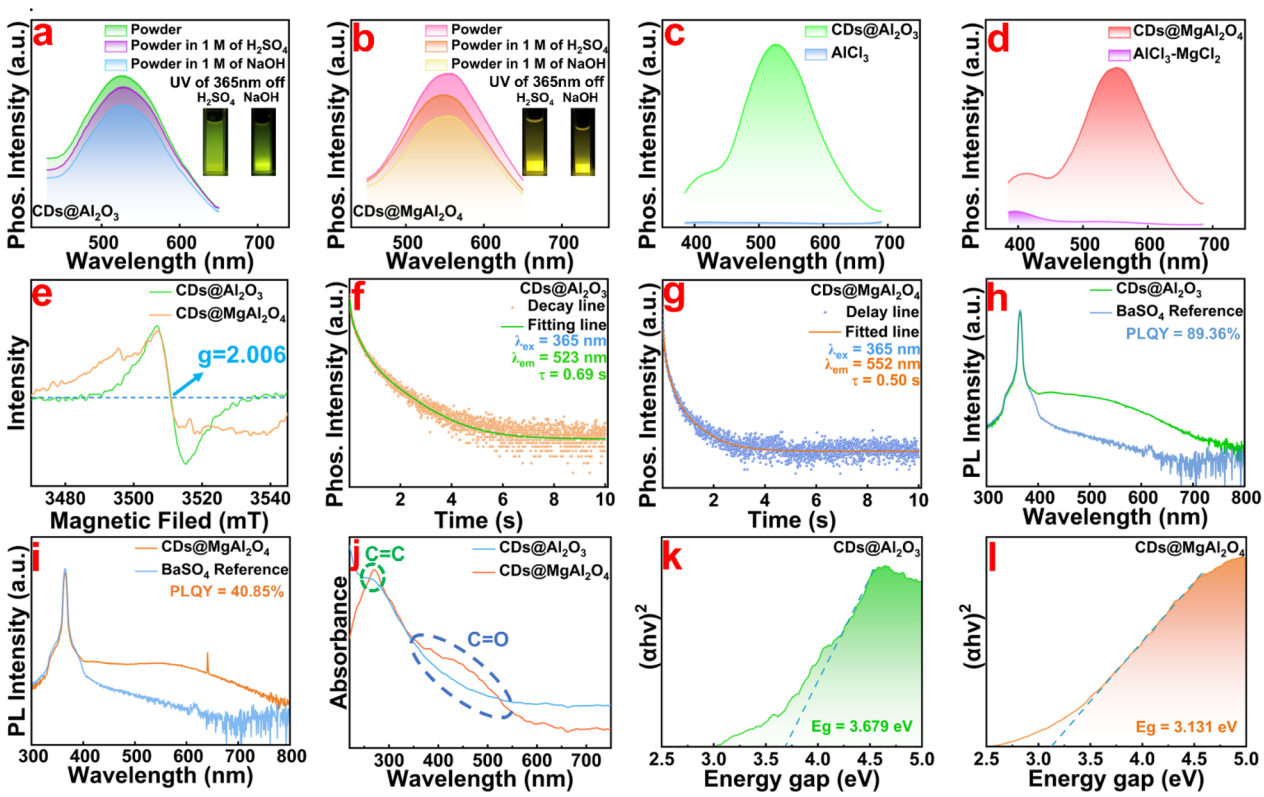

Fig. 3 Phosphorescence spectra of (a) CDs@Al_2O_3 and (b) CDs@$MgAl_2O_4$ without and with 1 M H_2SO_4 or 1 M NaOH. Phosphorescence spectra of (c) CDs@Al_2O_3 and $AlCl_3$ and (d) CDs@$MgAl_2O_4$ and $AlCl_3$–$MgCl_2$. (e) EPR spectra of CDs@Al_2O_3 and CDs@$MgAl_2O_4$. Time-resolved phosphorescence decay curve of (f) CDs@Al_2O_3 and (g) CDs@$MgAl_2O_4$. Photoluminescence quantum yield of (h) CDs@Al_2O_3 and (i) CDs@$MgAl_2O_4$. (j) UV-vis absorption spectra of CDs@Al_2O_3 and CDs@$MgAl_2O_4$. Diffuse reflectance spectra of (k) CDs@Al_2O_3 and (l) CDs@$MgAl_2O_4$.

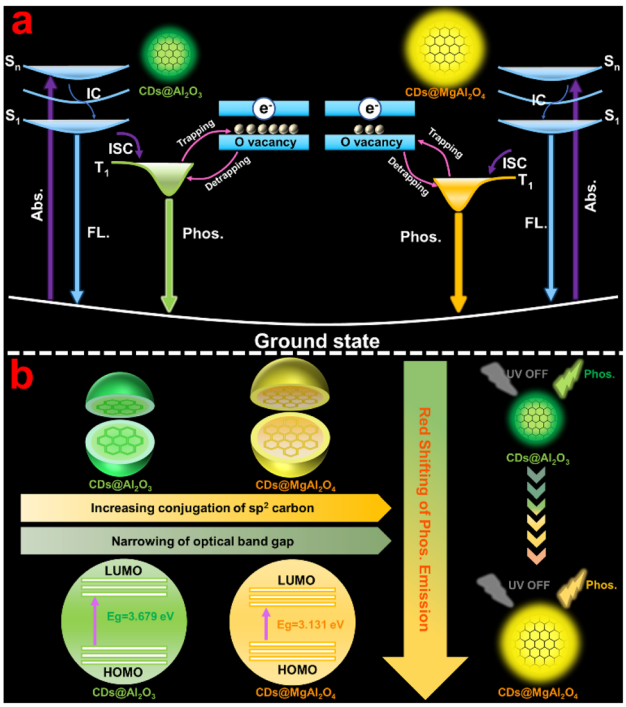

Fig. 4 (a) Mechanism of achieving pronounced phosphorescence for $CDs@Al_2O_3$ and $CDs@MgAl_2O_4$. (b) Aspects of regulating the phosphorescence red-shift for $CDs@MgAl_2O_4$.

wavelengths, distinct phosphorescence emissions were observed for $CDs@Al_2O_3$ and $CDs@MgAl_2O_4$, whereas both the products without utilizing folic acid exhibited negligible afterglow (Fig. 3c and d). These results demonstrated that folic acid was necessarily responsible for achieving the phosphorescence.

Meanwhile, electron paramagnetic resonance (EPR) was employed to investigate the presence of defects in the two CDs. In the EPR spectra of $CDs@Al_2O_3$ and $CDs@MgAl_2O_4$, both samples exhibited signals at $g = 2.006$, confirming the existence of oxygen vacancies (Fig. 3e).[35] To be specific, these oxygen vacancies served as effective trapping sites for triplet excitons, preventing their immediate transition to the electronic ground state (S_0). During the process of thermal disturbance, the trapped triplet excitons were released from the trap and gradually returned to the electronic ground state (S_0) through a radiative transition, thereby prolonging the lifetime and improving the quantum yield of phosphorescence.

Furthermore, the phosphorescence lifetime of $CDs@MgAl_2O_4$ was 0.50 s and the phosphorescence lifetime of $CDs@Al_2O_3$ was 0.69 s (Fig. 3f and g), revealing that both CDs possess relatively long phosphorescent lifetimes. Simultaneously, the photoluminescence (PL) quantum yields of $CDs@Al_2O_3$ and $CDs@MgAl_2O_4$ were calculated to be 89.36% and 40.85% under 365 nm excitation (Fig. 3h and i), demonstrating their high quantum yields for both CDs. These findings showed agreement with the data of EPR, indirectly providing evidence that oxygen vacancy-mediated defects were critical for prolonging the lifetime and promoting the quantum yield of phosphorescence. Based on the overlap ratios between photoluminescence and phosphorescence spectra, the phosphorescence quantum yields of the two CDs were also determined to be 9.46% and 6.06%, respectively (Fig. S4 and S5).

In the UV-vis absorption spectra (Fig. 3j), $CDs@Al_2O_3$ exhibited a characteristic absorption peak at 275 nm, corresponding to the π–π^* transition of conjugated C=C within the carbon core. In contrast, $CDs@MgAl_2O_4$ not only displayed a primary absorption peak at 280 nm, but also showed an obvious shoulder peak at 380 nm that extended into the visible-light region. This shoulder peak was ascribed to the n–π^* transition of C=O coordinated with magnesium, thus enhancing the light absorption capacity of C=O by altering the electron cloud through metal coordination.[32]

To obtain the optical band gap (E_g) between the highest occupied molecular orbital (HOMO) and the lowest unoccupied molecular orbital (LUMO) of $CDs@Al_2O_3$ and $CDs@MgAl_2O_4$, we further recorded their UV diffuse reflectance spectra. By analyzing the Tauc plot, we calculated their E_g to be 3.679 and 3.131 eV, respectively (Fig. 3k and j). The narrowed band gap of $CDs@MgAl_2O_4$ ($\Delta E_g = 0.548$ eV) was ascribed to the introduction of magnesium. In brief, the magnesium with a high charge density led to a rearranged electron cloud and a decreased HOMO–LUMO band gap,[36] resulting in the red-shifted phosphorescence of $CDs@MgAl_2O_4$ compared with $CDs@Al_2O_3$. Furthermore, the DFT calculations further confirmed that the band gap of the magnesium-doped CDs showed a similar narrowing trend, consistent with the experimental results (Fig. S9).

Taken together, once $CDs@Al_2O_3$ and $CDs@MgAl_2O_4$ were irradiated with a light source, the electrons of the ground state (S_0) were excited to higher singlet states (S_n) followed by non-radiative transitions to S_1, and subsequently underwent ISC to the triplet state T_1. The triplet state electrons were captured by oxygen vacancies, and the trapped triplet excitons were then released from these oxygen vacancies, and this process prolonged their phosphorescence lifetime and improved their quantum yields, thus emitting long-lived and strong phosphorescence (Fig. 4a). Furthermore, the phosphorescence red-shift of $CDs@MgAl_2O_4$ was mainly due to the increased conjugation extent of sp^2 carbon and the narrowed optical band gap. These synergistic effects of the two aspects resulted in the pronounced phosphorescence red-shift of $CDs@MgAl_2O_4$ compared with that of $CDs@Al_2O_3$ (Fig. 4b).

To prove the universality of this strategy, we selected more carbon sources including L-glutamic acid, glycine, succinic acid, phthalimide and tartaric acid, all of which contained abundant C=O, to synthesize a series of CDs by the same approach of preparing $CDs@Al_2O_3$ and $CDs@MgAl_2O_4$. These CDs were named according to their raw materials, which included L-Glu-$CDs@Al_2O_3$ and L-Glu-$CDs@MgAl_2O_4$ (Fig. 5a and f), Gly-$CDs@Al_2O_3$ and Gly-$CDs@MgAl_2O_4$ (Fig. 5b and g), SA-$CDs@Al_2O_3$ and SA-$CDs@MgAl_2O_4$ (Fig. 5c and h), Phth-$CDs@Al_2O_3$ and Phth-$CDs@MgAl_2O_4$ (Fig. 5d and i), and TA-$CDs@Al_2O_3$ and TA-$CDs@MgAl_2O_4$ (Fig. 5e and j). Under identical conditions, all these CDs exhibited intense phosphorescence under 365 nm excitation. Similarly, the magnesium-doped CDs demonstrated an obvious red-shift in their phosphorescence emission spectra compared with the CDs without

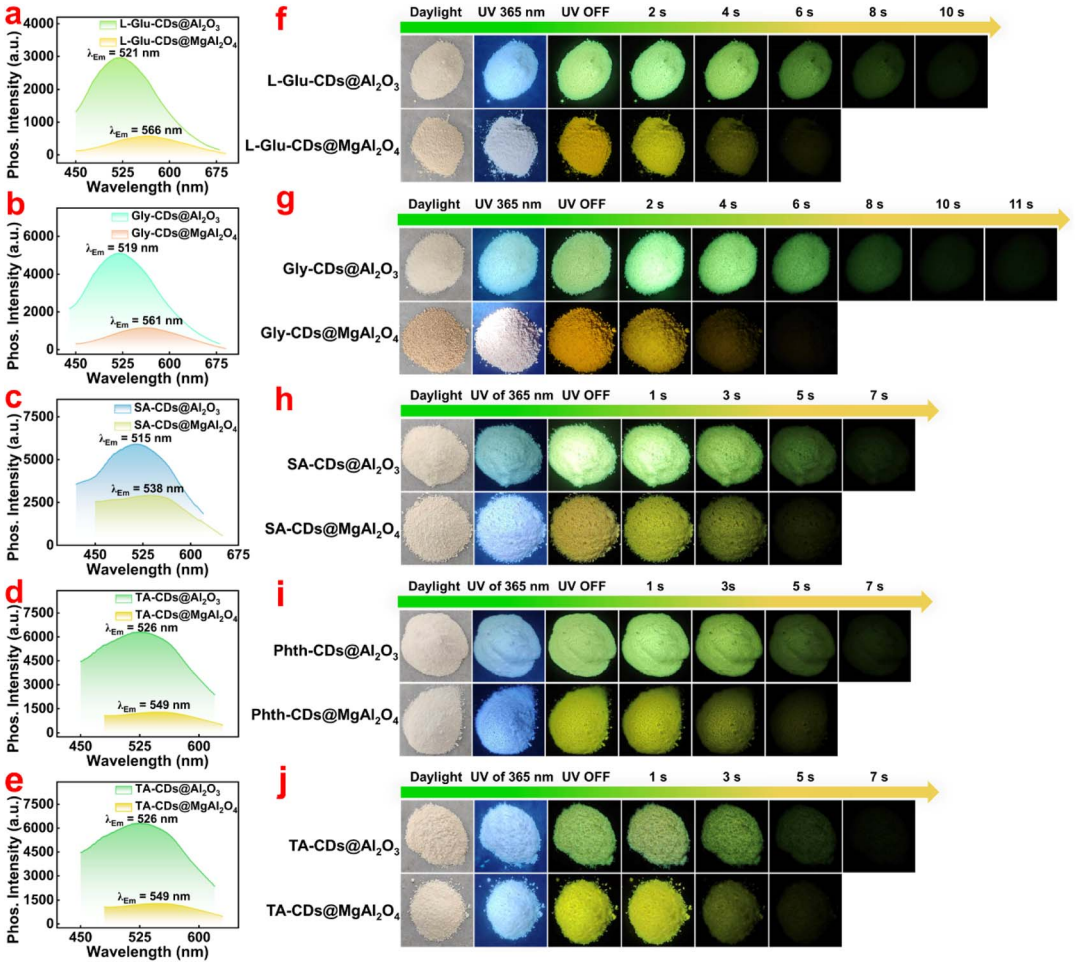

Fig. 5 Phosphorescence emission spectra of (a) L-Glu-CDs@Al_2O_3 and L-Glu-CDs@$MgAl_2O_4$, (b) Gly-CDs@Al_2O_3 and Gly-CDs@$MgAl_2O_4$, (c) SA-CDs@Al_2O_3 and SA-CDs@$MgAl_2O_4$, (d) Phth-CDs@Al_2O_3 and Phth-CDs@$MgAl_2O_4$, and (e) TA-CDs@Al_2O_3 and TA-CDs@$MgAl_2O_4$. (f–j) The corresponding images under daylight, 365 nm UV irradiation and after the UV light was turned off.

magnesium, which suggested the broad universality of this strategy.

3. Conclusions

In summary, we have successfully designed and prepared CDs@Al_2O_3 and CDs@$MgAl_2O_4$ with multiple-color phosphorescence and excellent pH tolerance by an *in situ* preparation strategy. Owing to the oxygen vacancy defects formed, both CDs@Al_2O_3 and CDs@$MgAl_2O_4$ achieved long-lived and high quantum-yield phosphorescence. Significantly, the incorporation of magnesium in CDs@$MgAl_2O_4$ significantly enhanced its red-shifted phosphorescence. Additionally, the phosphorescence of CDs@Al_2O_3 and CDs@$MgAl_2O_4$ was excitation-dependent, and multiple-color phosphorescence could be realized by regulating the excitation wavelength. Through changing the carbon sources, we further synthesized a series of CDs with distinct phosphorescence, demonstrating the universality of this strategy and providing an innovative approach for designing CD-based multicolor phosphorescent materials.

4. Experimental section

4.1. Chemicals and materials

Folic Acid (FA) was purchased from Heowns Biochem Technologies LLC (Tianjin, China). $AlCl_3 \cdot 6H_2O$, tartaric acid and succinic acid were acquired from Macklin Biochemical Co., Ltd (Shanghai, China), while $MgCl_2$ was from Bide Pharmatech Co., Ltd (Shanghai, China). NH_3 H_2O was purchased from Chongqing Chuandong Chemical (Group) Co., Ltd (Chongqing, China). Phthalimide was purchased from Aladdin Reagent Co., Ltd (Shanghai, China) and L-glutamic acid and glycine were purchased from Chron Chemicals Co., Ltd (Chengdu, China). In addition, all the commercial reagents were utilized directly without further purification, and ultrapure water produced using an Aquapro AWL-0502-P water system (18.25 MΩ cm) was employed throughout the entire experimental procedure.

4.2. Characterization

The synthesis of CDs@Al_2O_3 and CDs@$MgAl_2O_4$ was performed in a ZSX 1200 muffle furnace (Beijing, China). The fluorescence and phosphorescence spectra were recorded using a Hitachi F-

7000 fluorescence spectrophotometer (Tokyo, Japan), and UV-vis absorption was recorded with a Shimadzu UV-3600i Plus ultraviolet-visible spectrophotometer (Tokyo, Japan). The morphology was characterized using a JEOL JEM-F200 high-resolution transmission electron microscope (HR-TEM) (Tokyo, Japan) operating at 200 kV. Meanwhile, X-ray photoelectron spectroscopy (XPS) of CDs@Al_2O_3 and CDs@$MgAl_2O_4$ was performed using a Thermo Scientific K-Alpha X-ray photoelectron spectrometer (New York, America), and X-ray diffraction (XRD) patterns were acquired using a Rigaku Ultima IV X-ray diffraction analyzer. The surface groups of CDs were examined through a Fourier transform infrared (FTIR) spectrometer (Tokyo, Japan). The phosphorescence spectra, quantum yields and lifetime measurements were performed using an Edinburgh FLS1000 photoluminescence spectrophotometer (Edinburgh, Scotland) equipped with a microsecond flash lamp (lF900, 100–0.1 Hz) and a time-gating device (delay time ranging from 0.001 to 9999 ms). Again, the Electron paramagnetic Resonance (EPR) spectra were recorded on an EPR spectrometer (Bruker EMXplus-9.5/12) operating at X-band frequencies ($\approx$9.846 GHz) and room temperature.

4.3. Synthesis of CDs@Al_2O_3 and CDs@$MgAl_2O_4$

During the synthesis, 0.1 mmol of folic acid (FA) and 8 mmol of $AlCl_3 \cdot 6H_2O$ were mixed with 3 mL of ultrapure water. Then, 5 mL NH_3 H_2O was slowly added to the mixed solution with stirring, and the mixture was dried at 60 °C for 12 h after the uniform stirring. Finally, the dried raw product was ground into a fine powder and calcined in air in a muffle furnace at 530 °C for 150 min at a rate of 5 °C/min to obtain CDs@Al_2O_3. Similarly, CDs@$MgAl_2O_4$ was synthesized using 0.1 mmol of folic acid, 4 mmol of $MgCl_2$ and 8 mmol of $AlCl_3 \cdot 6H_2O$ through the same way as CDs@Al_2O_3.

4.4. DFT calculations

The DFT method was applied to explore the configuration and mechanism. A finite ring model of graphene was chosen in the present work, where Al^{3+} ions and Mg^{2+} ions presented different coordination. DFT and plane wave basis sets were used to calculate the energy and were implemented in the Vienna *ab initio* Simulation Package (VASP). The projection enhanced wave (PAW) method was used to deal with the nuclear valence electron interaction. The generalized gradient approximation (GGA) of Perdew–Burke–Ernzerhof (PBE) was used to approximate the electronic changes and correlations. The convergence criterion of the electron self-consistent loop was 10^{-5} eV, and the ion relaxation converged to a force tolerance of less than 0.05 eV $Å^{-1}$.

Author contributions

Y. L. and H. Z. contributed to investigation and formal analysis. Y. C. was responsible for supervision and DFT calculations. X. Y. was responsible for supervision and wrote the original draft. All authors contributed to reviewing and editing the manuscript, and approved the final version of the manuscript.

Conflicts of interest

There are no conflicts to declare.

Data availability

The data that support the findings of this work have been included in the main text and supplementary information (SI). Supplementary information is available. See DOI: https://doi.org/10.1039/d5sc09281g.

Acknowledgements

This work was financially supported by Natural Science Foundation of Chongqing, China (CSTB2024NSCQ-MSX0417).

References

1 X. Luo, B. Tian, Y. Zhai, H. Guo, S. Liu, J. Li, S. Li, T. D. James and Z. Chen, Room-temperature phosphorescent materials derived from natural resources, *Nat. Rev. Chem.*, 2023, **7**, 800–812.
2 W. J. Zhao, Z. K. He and B. Z. Tang, Room-temperature phosphorescence from organic aggregates, *Nat. Rev. Mater.*, 2020, **5**, 869–885.
3 S. J. Zhou, F. X. Wang, N. Feng, A. X. Xu, X. F. Sun, J. Zhou and H. G. Li, Room Temperature Phosphorescence Carbon Dots: Preparations, Regulations, and Applications, *Small*, 2023, **19**, 2301240.
4 B. Chang, J. Chen, J. Bao, T. Sun and Z. Cheng, Molecularly Engineered Room-Temperature Phosphorescence for Biomedical Application: From the Visible toward Second Near-Infrared Window, *Chem. Rev.*, 2023, **123**, 13966–14037.
5 L. Dordevic, F. Arcudi, M. Cacioppo and M. Prato, A multifunctional chemical toolbox to engineer carbon dots for biomedical and energy applications, *Nat. Nanotechnol.*, 2022, **17**, 112–130.
6 B. Wang, J. Wang and S. Lu, Carbon Dots: Small Materials With Big Impacts on Optoelectronic Devices, *Aggregate*, 2025, **6**, e70212.
7 B. Wang, G. I. N. Waterhouse, B. Yang and S. Lu, Advances in Shell and Core Engineering of Carbonized Polymer Dots for Enhanced Applications, *Acc. Chem. Res.*, 2024, **57**, 2928–2939.
8 Y. You and W. Nam, Photofunctional triplet excited states of cyclometalated Ir(III) complexes: beyond electroluminescence, *Chem. Soc. Rev.*, 2012, **41**, 7061–7084.
9 X. Yang, X. Lin, Y. Zhao, Y. S. Zhao and D. Yan, Lanthanide Metal–Organic Framework Microrods: Colored Optical Waveguides and Chiral Polarized Emission, *Angew. Chem., Int. Ed.*, 2017, **56**, 7853–7857.
10 X. Zhang, L. Du, W. Zhao, Z. Zhao, Y. Xiong, X. He, P. F. Gao, P. Alam, C. Wang, Z. Li, J. Leng, J. Liu, C. Zhou, J. W. Y. Lam, D. L. Phillips, G. Zhang and B. Z. Tang, Ultralong UV/mechano-excited room temperature phosphorescence from purely organic cluster excitons, *Nat. Commun.*, 2019, **10**, 5161.

11 L. Wang, W. Li, L. Yin, Y. Liu, H. Guo, J. Lai, Y. Han, G. Li, M. Li, J. Zhang, R. Vajtai, P. M. Ajayan and M. Wu, Full-color fluorescent carbon quantum dots, *Sci. Adv.*, 2020, **6**, eabb6772.
12 X. B. Huang, X. L. Jin, H. Y. Bai, B. Huang, X. Y. Zhang, J. L. Zuo, X. H. Ma, L. Ding, H. W. Zhou, X. Feng and W. X. Chen, Highly Efficient Wavelength Red-Shift Regulating Strategy of Carbon Dots Composites *via* the Effective Conjugated Domain and the Hydrogen Bonding Synergy, *Adv. Mater.*, 2025, **37**, 2418335.
13 Y. Zhang, Y. Liu, X. Ren, Y. Kang, S. Ding and S. Lu, Adjusting TADF and Phosphorescence for Tailored Dynamic Time-Dependent Afterglow Colored Carbon Dots spanning Full Visible Region, *Angew. Chem., Int. Ed.*, 2025, **64**, e202421421.
14 H. Wu, Y. Kang, S. Jiang, K. Wang, L. Qu and C. Yang, Hectogram-Scale Synthesis of Visible Light Excitable Room Temperature Phosphorescence Carbon Dots, *Small*, 2024, **20**, 2402796.
15 Y. Jiang, T. Zhao, W. Xu and Z. Peng, Red/NIR C-dots: A perspective from carbon precursors, photoluminescence tuning and bioapplications, *Carbon*, 2024, **219**, 118838.
16 W. B. Zhao, K. K. Liu, Y. Wang, F. K. Li, R. Guo, S. Y. Song and C. X. Shan, Antibacterial Carbon Dots: Mechanisms, Design, and Applications, *Adv. Healthcare Mater.*, 2023, **12**, 2300324.
17 C. Kang, S. Tao, F. Yang, C. Zheng, Z. Qu and B. Yang, Enabling Carbonized Polymer Dots with Color-tunable Time-dependent Room Temperature Phosphorescence through Confining Carboxyl Dimer Association, *Angew. Chem., Int. Ed.*, 2024, **63**, e202316527.
18 H. Hu, J. Li and X. Gong, Hour-Level Persistent Multicolor Phosphorescence Enabled by Carbon Dot-Based Nanocomposites Through a Multi-Confinement-Based Approach, *Small*, 2024, **20**, 2308457.
19 Y. Bi, J. Yu, J. Xiao, K. Zhu, B. Wang, X. Xu and S. Lu, Visible Light Excited Time-Dependent Phosphorescence Color Tuning in Carbon Dots *via* Charge Transfer, *Angew. Chem., Int. Ed.*, 2025, **64**, e202506162.
20 W. Li, W. Zhou, Z. S. Zhou, H. R. Zhang, X. J. Zhang, J. L. Zhuang, Y. L. Liu, B. F. Lei and C. F. Hu, A Universal Strategy for Activating the Multicolor Room-Temperature Afterglow of Carbon Dots in a Boric Acid Matrix, *Angew. Chem., Int. Ed.*, 2019, **58**, 7278–7283.
21 L. Ai, W. Xiang, J. Xiao, H. Liu, J. Yu, L. Zhang, X. Wu, X. Qu and S. Lu, Tailored Fabrication of Full-Color Ultrastable Room-Temperature Phosphorescence Carbon Dots Composites with Unexpected Thermally Activated Delayed Fluorescence, *Adv. Mater.*, 2024, **36**, 2401220.
22 B. Y. Wang and S. Y. Lu, The light of carbon dots: From mechanism to applications, *Matter*, 2022, **5**, 110–149.
23 S. Y. Song, K. K. Liu, X. Mao, Q. Cao, N. Li, W. B. Zhao, Y. Wang, Y. C. Liang, J. H. Zang, X. Li, Q. Lou, L. Dong and C. X. Shan, Colorful Triplet Excitons in Carbon Nanodots for Time Delay Lighting, *Adv. Mater.*, 2023, **35**, 2212286.
24 H. Liu, X. Zhong, Q. Pan, Y. Zhang, W. Deng, G. Zou, H. Hou and X. Ji, A review of carbon dots in synthesis strategy, *Coord. Chem. Rev.*, 2024, **498**, 215468.
25 J. Li, H. Zhou, S. Jin, B. Xu, Q. Teng, C. Li, J. Li, Q. Li, Z. Gao, C. Zhu, Z. Wang, W. Su and F. Yuan, Achieving Bright and Long-Lived Aqueous Room-Temperature Phosphorescence of Carbon Nitrogen Dots Through *In Situ* Host–Guest Binding, *Adv. Mater.*, 2024, **36**, 2401493.
26 Z. Guo, C. Wang, F. Qi, J. Dong, J. Xue, Y. Zhang, B. Xu, G.-N. Liu, Y. Sun and C. Li, Sunlight-Activated Room-Temperature Phosphorescent Carbon Dots, *Adv. Funct. Mater.*, 2024, **35**, 2414178.
27 Y. Zhang, L. Chen, B. Liu, S. Yu, Y. Yang and X. Liu, Multicolor Afterglow Carbon Dots: Luminescence Regulation, Preparation, and Application, *Adv. Funct. Mater.*, 2024, **34**, 2315366.
28 J. Xu, Q. Liang, Z. Li, V. Y. Osipov, Y. Lin, B. Ge, Q. Xu, J. Zhu and H. Bi, Rational Synthesis of Solid-State Ultraviolet B Emitting Carbon Dots *via* Acetic Acid-Promoted Fractions of sp3 Bonding Strategy, *Adv. Mater.*, 2022, **34**, 2200011.
29 K. Fu, X. Liu, Y. Yang, Z. Wang, W. Zhou, G. Tong, X. Wang and W. Wu, Synchronously enhanced electromagnetic wave absorption and heat conductance capabilities of flower-like porous γ-Al_2O_3@Ni@C composites, *Chem. Eng. J.*, 2023, **457**, 141318.
30 C. Feng, D. Ding, G. Xiao, C. Lei, X. Chong, L. Lv and E. Jin, One-step synthesis of CNTs/MAw hybrids with excellent water wettability: The fate and role of Fe catalyst in growth of CNTs and $MgAl_2O_4$ whiskers, *Carbon*, 2025, **234**, 119984.
31 Y. Ma, L. Wu, X. Ren, Y. Zhang and S. Lu, Toward Kilogram-Scale Preparation of Full-Color Carbon Dots by Simply Stirring at Room Temperature in Air, *Adv. Funct. Mater.*, 2023, **33**, 2305867.
32 J. Shi, J. Li, X. Li, Y. Zhang, J. Hu, Y. Ning, C.-H. Zhou, Z. Xia and C. Liu, Coordination of Mg(II) Enhancing Photoinduced Oxidase-Like Activity of Carbon Dots for Efficient Degradation of Organic Dyes, *Chem. Mater.*, 2025, **37**, 2290–2301.
33 Y. Z. Liu, D. Liu, X. Han, Z. P. Chen, M. Li, L. W. Jiang and J. G. Zeng, Magnesium-Doped Carbon Quantum Dot Nanomaterials Alleviate Salt Stress in Rice by Scavenging Reactive Oxygen Species to Increase Photosynthesis, *ACS Nano*, 2024, **18**, 31188–31203.
34 B. Liu, M. Cai, X. Feng, S. Lu, S. Lin and F. Tian, Enzyme-free carbon dots@MgO nanocomposite as an efficient sensor for on-site detection and degradation of paraoxon toxins, *Carbon*, 2023, **209**, 118003.
35 Y. B. Shi, H. W. Shou, H. Li, G. M. Zhan, X. P. Liu, Z. P. Yang, C. L. Mao, J. D. Cheng, X. Zhang, Y. Q. Jiang, S. X. Zhao, J. X. Wang, X. Liu, L. Song, H. W. Sun and L. Z. Zhang, Visible Light-Driven Conversion of Carbon-Sequestrated Seawater into Stoichiometric CO and HClO with Nitrogen-Doped BiOCl Atomic Layers, *Angew. Chem., Int. Ed.*, 2023, **62**, e202302286.
36 J. Sun, Y. C. Liu, Y. D. Han, W. H. Li, N. Wang, L. Zhang, Y. Zhang, F. Y. Deng, D. S. Wang and X. Zhang, Enabling controllable time-dependent phosphorescence in carbonized polymer dots based on chromophore excited triplet energy level modulation by ionic bonding, *Angew. Chem., Int. Ed.*, 2025, **64**, e202415042.